

Effect of density ratio on the secondary breakup: A numerical study

Suhas. S. Jain^{*}, R. Suryaprakash, B. N. Raghunandan, R. V. Raviskrishna, Gaurav. Tomar[†]
Department of Mechanical Engineering, Indian Institute of Science, India

Abstract

Secondary atomization has been the subject of interest for many decades - a phenomenon that is widely seen in both natural as well as industrial environments. While there have been several experimental studies at ambient conditions which involve real-world density ratios ($\rho^* = \rho_{liq}/\rho_{gas} > 500$), most of the numerical investigations have been at much lower density ratios ($\rho^* < 50$). Present study attempts to bridge this gap by studying the single drop breakup behavior for a wide range of density ratios (10-1000) using fully resolved volume-of-fluid (VOF) simulations. It is well established that the non-dimensional parameter, aerodynamic Weber number (We) dictates the regimes of secondary breakup. Therefore, both ρ^* and We are varied independently to capture different regimes of droplet breakup for different ρ^* at a given We . A phase plot of $\rho^* - We$ is also plotted showing the different regimes of breakup. We show that the breakup dynamics of the droplets at low density ratios is significantly different to that observed at high density ratios. We also study the temporal characteristics of the droplet deformation and motion.

Introduction

When a drop is accelerated in a high speed gas flow, it deforms due to the aerodynamic forces and eventually fragments into tiny droplets; this is termed as secondary breakup. This phenomenon has been studied over many decades in the interest of its numerous applications, for example, in rainfall, sprays, combustion and chemical industries. Complete understanding of the breakup phenomenon is essential for an accurate determination of the drop size distribution which dictates the surface to volume ratio and hence the efficiency of drying, chemical reaction and combustion. Further, a better understanding of the breakup also helps in developing accurate closure relations for Lagrangian and Eulerian Multi-Fluid modeling approaches.

Over the years, numerous experimental and numerical studies have been performed to study secondary breakup of a drop. Several articles ([1, 2, 3]) have periodically reviewed the advances in this field. The secondary breakup of a drop can be broadly categorized into four modes of deformation and breakup, primarily based on the aerodynamic Weber number and liquid Ohnesorge number: (a) Vibrational mode, where a drop oscillates at its natural frequency and it may (or may not) undergo breakup [4] and when it breaks it produces fewer daughter drops of the size comparable to that of the parent drop [1], (b) Bag mode, where a drop deforms into a flat disc and then is blown into a thin bag, attached to a toroidal ring, that expands and eventually ruptures, followed by the breakup of the toroidal ring [5, 6]. (c) Sheet thinning mode for higher Weber number, where the ligaments and small daughter drops break off from the thinning rim of the parent drop until the core of the parent drop reaches a stable state. (d) Catastrophic mode, where a drop breaks up into multiple fragments due to unstable surface waves at high speeds [7]. The transition of this breakup mode, as a function of Weber number, occurs very gradually (see Figure 5). Different authors have proposed different transitional values of We (subject to the inaccuracies in the exact calculation of We and also the presence of impurities that alter the properties of the fluid used in the experiments; see Table 1 in [8]) and hence the reliability of the transitional values of We has remained a moot point. Other parameters that influence the breakup mechanism are density ratio and gas Reynolds number (and liquid Ohnesorge number).

Several experimental studies have been performed in the last decades to unravel the physics of secondary breakup of droplets (see [3, 8] for an elaborate review). Some of the studies have been performed at low density ratio (in the range 1 – 10) while most of the studies have been performed for water-air systems.

Most of the numerical studies have been performed with low density ratios and only a few with high density ratio. Efforts in numerical studies have only started to pay off recently and most numerical simulations attempt to study the breakup at low density ratios ($\rho^* < 100$), essentially due to numerical convergence issues at high density ratios. Nevertheless, these studies find direct applications in high-pressure environment applications as well as in manufacturing of metal pellets by quenching liquid metal droplets. [9] performed one of the earliest numerical studies on the secondary breakup of drops in 2D. They observed a backward-bag at low Weber number (We) for $\rho^* = 10$ and reported that their results contradict the general experimental observation (which was mostly done

^{*}Present address: Department of Mechanical Engineering, Stanford University, USA.

[†]Corresponding author: gtom@iisc.ac.in

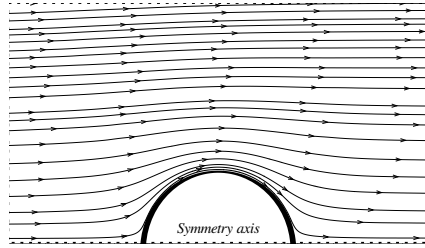


Figure 1: Schematic of the simulation setup (not drawn to scale). Flow direction represents the direction of the gas flow. Drop is shown at the initial time ($t = 0$).

for higher ρ^* values), where a forward-bag is seen at this We . They suggested that this mismatch is a result of the discrepancy in their initial conditions. [10] extensively studied the breakup of drops for two ρ^* values, 1.15 and 10. For $\rho^* = 10$, they observed a forward-bag at low We and backward-bag at higher We , and for $\rho^* = 1.15$ they observed backward-bag for all moderate We . They concluded that the formation of forward-bag is due to the detachment of the wake downstream of the drop and the formation of backward-bag is due to the entrapment of the drop in the vortex ring. On decreasing Re , they also observed that a higher We is required to obtain the same mode of breakup. [11] reported that the secondary atomization is essentially independent for $\rho^* > 32$ and that there is no effect of Re on We_{crit} beyond $Re > 100$. [12] studied the breakup of drops for $\rho^* = 20, 40$ and 80 and reported to have observed new breakup modes such as Bag, Shear, Jellyfish shear, thick rim shear, thick rim bag, rim shear and mixed. The new breakup modes were due to the influence of the viscous effects in their simulations (some of these cases are at $Oh \gg 0.1$ and $Re_g < 100$). [13] also studied the effect of ρ^* on the breakup but at a very high $We = 225$ value in the regime of catastrophic breakup for $\rho^* = 10, 25, 32, 60$. On decreasing ρ^* , they observed a lower deformation rate but the range of ρ^* values chosen was probably too low at such high We to see any discernible effect of changing ρ^* on the breakup. Formation of spherical cap and ligaments and the fragmentation of ligaments further into multiple drops were the common features they observed in their study. Recently, 3D simulations were performed for water and air at atmospheric conditions ($\rho^* \sim 1000$) by [14, 15]; but their main focus was to validate their LES code. We, in our previous work [6], have extensively studied the breakup and its characteristics for $\rho^* = 1000$ using fully resolved 3D simulations.

For the systems with low density ratios (< 100) and at moderate Weber numbers (20-80), backward-bag (opening of the bag facing the downstream direction followed by sheet thinning) has been seen as the predominant breakup mode in the numerical simulations (see [12, 16]). In the present work, we numerically study the effect of a wide range of density ratios on the drop breakup mechanisms at different aerodynamic Weber numbers.

Numerical Methods

Figure 1 shows the schematic of the computational domain for the axisymmetric simulations performed in this study with the dashed line marking the axis of symmetry. The domain is $10d_0$ along the radial direction and $20d_0$ along the axial direction, where d_0 is the diameter of the drop. Liquid and gas densities are ρ_l and ρ_g , respectively, and the ratio $\rho^* = \rho_l/\rho_g$ is varied from 10 to 1000 by keeping the gas density as unity and varying the liquid density. Viscosity of the liquid and the gas are given by μ_l and μ_g , respectively. Surface tension coefficient at the liquid-gas interface is given by σ .

For the simulations, gas inlet is at the left and is prescribed a uniform velocity of U_g , and outlet flow boundary conditions are imposed at the right end of the computational domain. Slip boundary conditions are applied at the other (side) walls of the domain to minimize the confinement effects and axisymmetric boundary conditions are imposed at the axis of symmetry marked by the dashed line in Figure 1. The drop is accelerated by the high-speed gas flow and its breakup is governed by the following five non-dimensional numbers: Aerodynamic Weber number $We = \rho_g U_g^2 d_0 / \sigma$, liquid Ohnesorge number $Oh = \mu_l / \sqrt{\rho d_0 \sigma}$, gas Reynolds number $Re = \rho_g U_g d_0 / \mu_g$, viscosity ratio $M = \mu_l / \mu_g$ and the density ratio $\rho^* = \rho_l / \rho_g$.

A one-fluid formulation is used for the numerical simulations [17]. The governing equations for the coupled liquid and gas flow simulated in this study are described in the following. Considering both the drop fluid and the surrounding gas to be incompressible, the corresponding continuity equation is given by $\nabla \cdot \mathbf{u} = 0$ where \mathbf{u} is the divergence free velocity field. The governing equations for the momentum conservation are given by the Navier–Stokes equations (Eqn. 1) along with the surface tension forces and the interfacial boundary conditions of

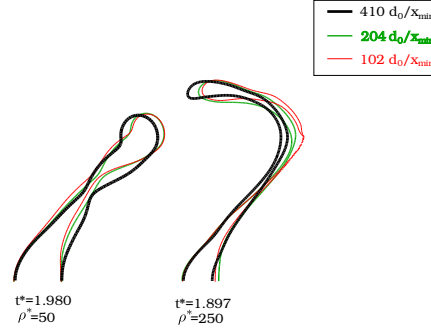


Figure 2: Drop shapes for $\rho^* = 50$ and 250 compared with profiles, obtained using grid resolutions 102, 204 and $410 d_0/\Delta x_{min}$, at the same time instant.

continuity of velocity, and normal and tangential stress balance:

$$\rho(C)\left(\frac{\partial \mathbf{u}}{\partial t} + \nabla \cdot \mathbf{u}\mathbf{u}\right) = -\nabla p + \nabla \cdot (2\mu(C)\mathbf{D}) + \sigma\kappa\mathbf{n}\delta_s. \quad (1)$$

Here, C is the volume fraction of liquid that takes a value of zero in the gas phase and one in the liquid phase. The density and viscosity for the one-fluid formulation are expressed as, $\rho = \rho_l C + \rho_g(1-C)$ and $\mu = \mu_l C + \mu_g(1-C)$, respectively. The deformation rate tensor is given by $D = (\nabla \mathbf{u} + (\nabla \mathbf{u})^T)/2$. The last term in the equation ($\sigma\kappa\mathbf{n}\delta_s$) accounts for the surface tension force ($\sigma\kappa$, where κ is the local interface curvature) and modeled using the continuum surface force approach [18]. The direction of this force is along the local normal (\mathbf{n}) at the interface. The evolution equation for the interface is given as an advection equation in terms of the volume fraction, C (obtained by applying kinematic boundary condition at the interface),

$$\frac{\partial C}{\partial t} + \mathbf{u} \cdot \nabla C = 0. \quad (2)$$

We use the adaptive mesh refinement (AMR) geometric volume of fluid (VOF) algorithm in Gerris [19, 20, 21] to solve the above set of equations. Gerris uses a second-order accurate staggered time discretization for velocity, volume-fraction and pressure fields. Balanced-force algorithm by [22] is used to accurately calculate the surface tension forces and minimize spurious currents. The discretization of the equations are described in detail in [19].

Adaptive mesh refinement (AMR) is performed using a cost function based on the local vorticity in the field and the gradient of the void-fraction field, thus using a very fine refinement in the regions of high velocity gradient and at the interface. We use 410 cells per diameter ($d_0/\Delta x_{min}$) of the initial spherical drop for the refinement of the interface and three different grid resolutions for the refinement of surrounding gas flow - 102, 204 and $410 d_0/\Delta x_{min}$ for our 2D axisymmetric simulations. This resolution is more than that employed in any of the previous studies in the literature. Figure 2 shows the drop shapes at different grid refinements and density ratios.

Drop shapes for grid resolutions 102, 204 and $410 d_0/\Delta x_{min}$ are identical (in a physically meaningful way), but we use the most fine mesh refinement of $410 d_0/\Delta x_{min}$ for all the axisymmetric simulations presented in this study. We also performed a few 3D simulations using a mesh refinement of $102 d_0/\Delta x_{min}$ to show the validity of our axisymmetric assumption [8].

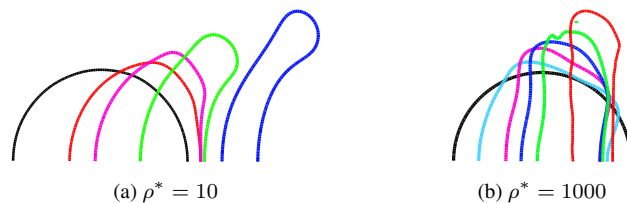
Results and Discussion

In order to investigate the effects of density ratio, ρ^* , on the secondary breakup of a drop, we perform a large set of well resolved simulations with different values of ρ^* and aerodynamic Weber number, We . Table 1 lists the parameter range covered in this study. The liquid Ohnesorge number for all the simulations is ≤ 0.1 and therefore the critical Weber number based on the previous studies [4, 23] is not expected to vary significantly.

In what follows, we discuss the effect of density ratio on the deformation and motion of the droplet. The time is non-dimensionalized with the characteristic time scale, $t^* = t/t_c$, where, $t_c = d_0\sqrt{\rho_l/\rho_g}/U_g$. Figure 3 shows the time evolution of the drop shape and the displacement for $\rho^* = 10$ and $\rho^* = 1000$ at $We = 20$. The flow of the gas is from left to right. Centroid of the drop for $\rho^* = 10$ moves a distance of $0.79d_0$, for $\rho^* = 200$ drop moves a distance of $0.48d_0$ (not shown in the figure) and for $\rho^* = 1000$ the drop moves a distance of $0.34d_0$ in $t^* = 1$. The leeward side of the drop for $\rho^* = 10$ also moves downstream with time, whereas the leeward side of the drop for $\rho^* = 1000$ remains virtually stationary until $t^* \sim 1$, though the centroid is moving in the

ρ^*	We	Re	M
10, 50, 100, 150, 200, 250, 500, 1000	20, 40, 60, 80, 100, 120	4000	100

Table 1: Parameters for the different simulations presented in this study.

Figure 3: Time evolution of the drop movement for $\rho^* = 10$ and $\rho^* = 1000$ at $We = 20$.

streamwise direction in both the cases. The significant difference in the motion of the centroid is primarily due to the differences in the velocity of the drop and the rate of momentum transmitted to the leeward side of the drop, which depends on the kinematic viscosity, ν . The value of ν for $\rho^* = 10$ is 100 times the ν for $\rho^* = 1000$. We can also observe the formation and motion of the capillary waves emanating from the rim of the drops in both the cases (more evidently for the drop at $\rho^*=1000$). Capillary time-scale based on inertia, also called as the Rayleigh time-scale [24], is given by $t_R \sim \sqrt{\rho_l d^3 / \sigma}$. This is around 3 times the characteristic time scale t_c of the drop in both the cases, since both t_c and t_R are proportional to $\sqrt{\rho_l}$. Capillary time-scale based on viscous forces is given by $t_M \sim \mu d / \sigma$. This is around 0.16 times t_c for the drop with $\rho^* = 10$ and around 0.016 times t_c for the drop with $\rho^* = 1000$, thus suggesting a lower resistance to the waves by the viscous forces in the case of high density ratio fluid relative to the low density case since ν is smaller. The stretching time-scale (for the rim) is obtained by the scaling $t_s \sim d / u_{rim}$. This is around 0.76 times the t_c for the drop with $\rho^* = 10$ and 1.12 times the t_c for the drop with $\rho^* = 1000$. Comparing these time scales, we note that the capillary reorganization occurs at a rapid rate in the high-density ratio case in comparison to the low density ratio cases. Further, the time scale for the stretching of the rim is significantly slower than the capillary wave time-scale for high density ratio cases. Therefore, for higher density ratio cases, a flat disc shape of the droplet is observed, whereas, for lower density ratios, drop progressively deforms into a backward bag without achieving a proper flat disc shape. Note that our definition of backward bag is the one where the rim of the bag is stretched in the direction of the flow relative to the bag. This is different from the one proposed by [25] but is consistent with the one used in [6, 26, 8].

Figure 4 shows the time evolution of the drop shapes for the cases where the drops do not breakup. Drop with $\rho^* = 10$ at $We = 20$ deforms into a concave-disc facing downstream and then bends in the opposite direction and finally collapses without breakup, encapsulating a bubble within it. For $We = 40$ and $\rho^* = 10$, it deforms into a backward-bag and again collapses onto itself before it could break. For $\rho^* = 50$ at $We = 20$, the drop deforms into a concave-disc facing downstream and then into the shape of a canopy-top. Subsequently, with further deformation of the drop, the rim tends to pinch-off from the core drop, but before it could pinch-off, the drop relaxes back collapsing onto itself without breakup. This also shows the highly complicated unsteady behavior of the evolution of drop shapes. To understand this behaviour of no-breakup, we calculate the instantaneous Weber number (based on the velocity of the gas relative to the drop velocity) at the onset of breakup using $We_{inst} = \rho_g (U_g - u_{drop})^2 d_0 / \sigma$. Estimating the centroid velocity of the drop u_{drop} from the simulations at $We = 20$, we find that the $We_{inst} = 3.69$ for $\rho^*=10$, $We_{inst} = 8.91$ for $\rho^*=50$ and $We_{inst} = 11.1$ for $\rho^*=100$, and We_{inst} increases further with increase in ρ^* value. Clearly for $\rho^* = 10$ and $\rho^* = 50$, We_{inst} is below the $We_{crit} \sim 10 - 12$, implying that the drop would not breakup. Similarly, at $We = 40$, $We_{inst} = 8.92$ for $\rho^*=10$ and $We_{inst} = 18.31$ for $\rho^*=50$. Here again for $\rho^*=10$, We_{inst} is below the We_{crit} whereas, for $\rho^*=50$, $We_{inst} > We_{crit}$ for an initial aerodynamic Weber number $We = 40$, and thus we observe breakup of the drop. These predictions based on the criterion $We_{inst} > We_{crit}$ for the breakup of drop are in good agreement with our numerical results (as also shown in Figure 4). Thus, we can conclude that the breakup of a drop not only depends on the initial We value but also on the initial dynamics of the drop. More importantly, for low density ratio, for the same momentum transfer the relative velocity decreases much faster in comparison to the rates of deformation of the drop, thus, the instantaneous We decreases sharply and vibrational modes, without breakup, are observed.

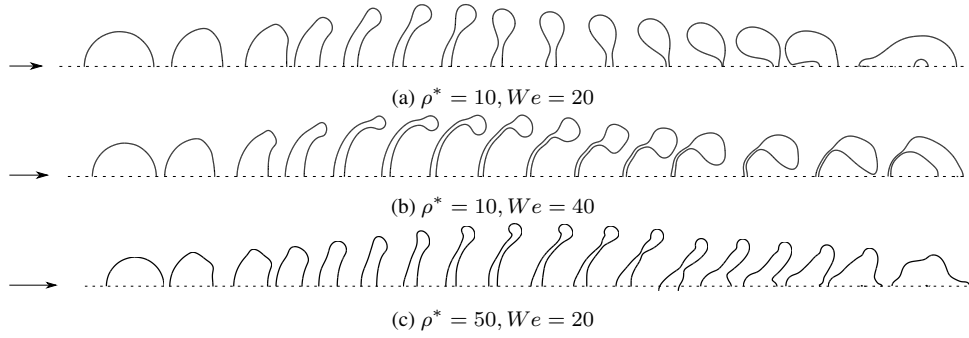


Figure 4: Evolution of the drop shape in time for $\rho^* = 10$ at $We=20, 40$ and $\rho^* = 50$ at $We = 20$. Arrows show the direction of gas flow and the dotted lines mark the axis of symmetry. Note that the distance between consecutive droplet profiles plotted here does not represent the actual displacement of the drop.

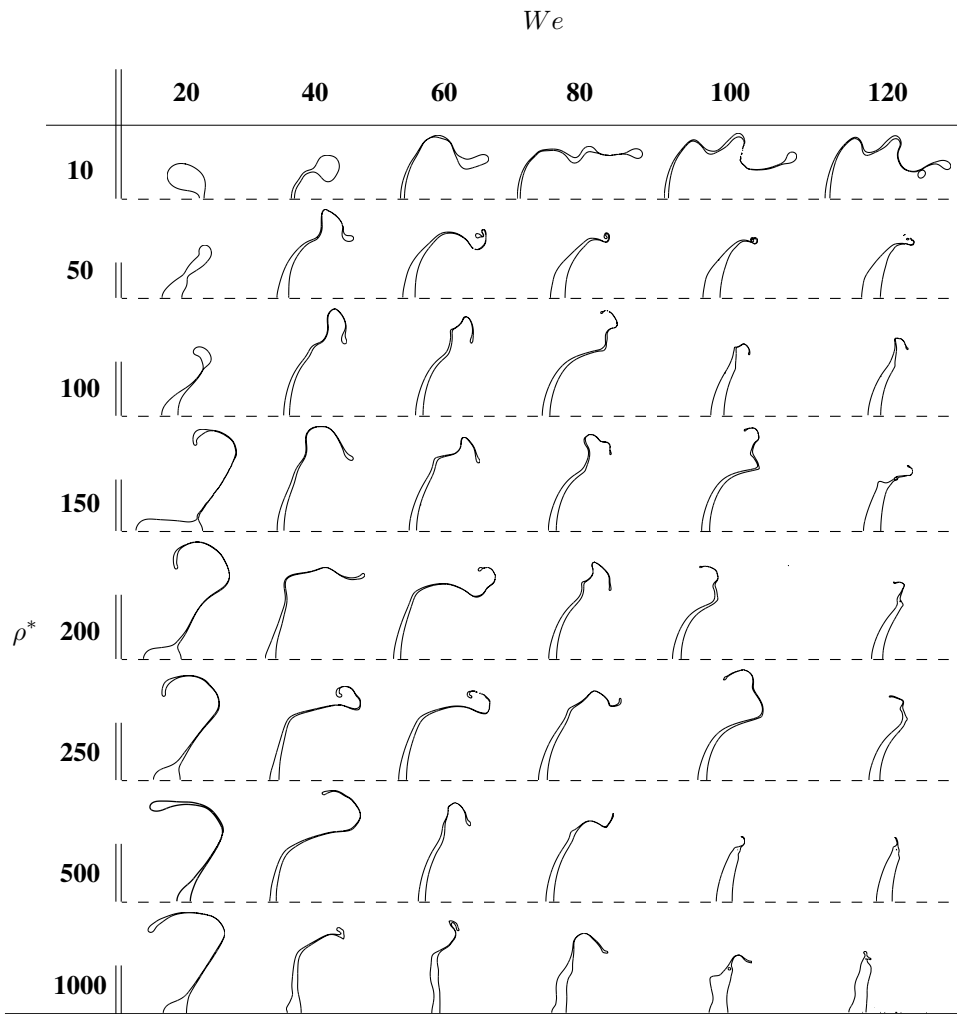


Table 2: Typical shapes of the drop at the onset of breakup for $\rho^* = 10 - 1000$ at $We = 20 - 120$, $Re_g = 4000$, $M = 100$ and $Oh = 0.003 - 0.9$. The time t_b^* where the profiles are taken is plotted in the Figure 6a.

In order to study the morphology of the drops during breakup, typical shapes of the drops at the onset of the breakup have been tabulated in Table 2 for all the conditions listed in the Table 1. Again, for the cases presented in the Figure 4, no breakup is observed. Comparing the drop shapes for different ρ^* values (for the same We)

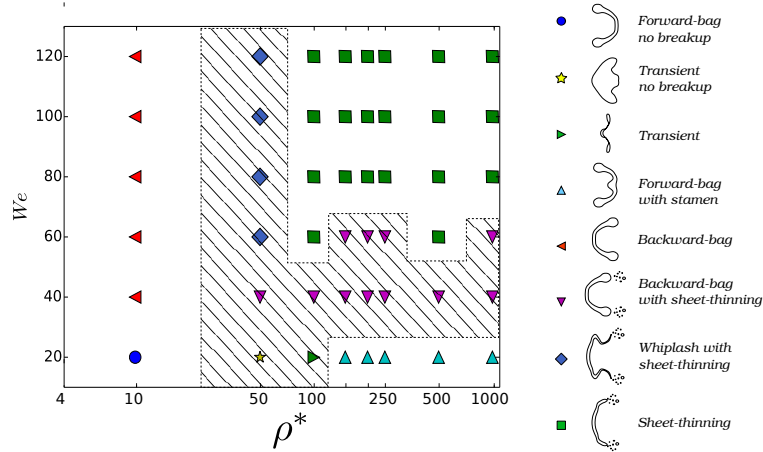


Figure 5: Phase plot $\rho^* - We$ along with the typical drop shapes for breakup modes shown on the right. Hatched region shows the transition regime. The ρ^* - axis is scaled to the logarithm base of 2.

in the Table 2 reveals that at $We = 20$, a forward-bag (facing the gas flow) is seen for $\rho^* = 10$, transient drop shapes (canopy-top which can also be seen as a shape in between forward-bag and backward-bag) for $\rho^* = 50$ and 100, and a forward-bag (bag facing the flow) with stamen for $\rho^* \geq 150$. For $\rho^* = 50$ and 100, the drop shapes are similar, but for $\rho^* = 50$ the rim does not pinch-off from the core drop whereas, for $\rho^* = 100$, the rim eventually pinches-off from the drop breaking into a toroidal ring and a smaller drop. There seems to be a progressive change with increase in ρ^* , from canopy shaped drop for $\rho^* = 50$ to a drop with not-so-clear stamen for $\rho^* = 100$ and very prominent stamen with a bag for $\rho^* > 150$. Interestingly, the stamen is very long for $\rho^* = 150$ and it decreases in size with increase in ρ^* . This is due to a higher relative velocity between the stamen and the drop for lower ρ^* which results in more stretching of the stamen at lower ρ^* values and hence results in the formation of a longer stamen. This forward-bag with stamen mode of breakup at $We = 20$ was observed before in [6] at $We = 40$. This difference in We may be due to the significantly different Oh used in [6] and in the present simulations, though in both the cases $Oh < 0.1$ was maintained. For example, the Oh used in [6] was 0.1 for $\rho^* = 1000$ in all the simulations, whereas here we use $Oh = 0.0035$ for a similar case of $\rho^* = 1000$ at $We = 20$. Gas Reynolds number used for $\rho^* = 1000$ discussed above is 4000, whereas [6] performed the simulations at $Re_g = 1414$. This effect of Oh on the drop deformation and breakup was discussed in more detail in [8].

At $We = 40$ and higher, a backward-bag is seen for $\rho^* = 10$ (as also observed by [10] for $\rho^* = 10$ at $Re = 242$ and $We \geq 37.4$), for $\rho^* = 50$ a transient form of sheet-thinning, where the thin rim oscillates like a whiplash (ensuing the motion from the vortex shedding in the surrounding gas flow) and for $\rho^* = 100$ and higher, drop deforms into a concave-disc (facing downstream) and eventually breaks up due to sheet-thinning. For $\rho^* = 200 - 1000$ at $We = 40$ and for $\rho^* = 200 - 250$ at $We = 60$, we see an interesting ‘‘cowboy-hat’’ shape of the drop. A similar drop shape was observed by [16]. For $\rho^* = 10$, the length of the rim increases with an increase in We value, whereas for higher ρ^* ($\rho^* = 100-1000$), the length of the rim decreases with increase in We and at the bottom-right corner of the table for $\rho^* = 500$ and 1000 at $We = 100$ and 120, the drops at the onset of breakup are essentially flat discs without any discernible rim. The length and the thickness of the rim is very small that results in the formation of very fine drops during sheet-thinning breakup. Another interesting observation is that the rim is thicker for drops of lower ρ^* . This is possibly due to higher Taylor-Culick velocity u_{tc} for lower ρ^* , where $u_{tc} = \sqrt{2\sigma/\rho_l h}$. Hence, a higher u_{tc} and a higher stretching velocity u_s at the rim (equal to the values of u_{rim} in Figure 4, and is of the order of the velocity given by $\sqrt{1/\rho^*}U_g$ and acts in the opposite direction to u_{tc}), result in the formation of a swollen rim for the drops with lower ρ^* . Consequently, the stretching of the fluid in this swollen rim takes more time resulting in the delayed breakup/pinch-off of the rims of the drops for low ρ^* values. This is also in agreement with our observed breakup time, t_b^* , for $\rho^* = 10$ case as shown later in the Figure 6a.

To summarize the breakup modes presented in the Table 2, we draw a phase plot of ρ^* vs We shown in the Figure 5. Typical shapes for each breakup mode is shown beside the plot. Hatched region marks the transition regime indicating transition from bag(forward/backward) to sheet-thinning.

In addition to these differences in the deformation, breakup morphologies and breakup modes, the breakup mechanism is also different for higher and lower ρ^* values. Breakup is due to the RT instability at higher ρ^* values ($\rho^* \geq 150$) [27, 6, 26, 8], whereas breakup is due to the dynamics of the rim at lower ρ^* values and is significantly

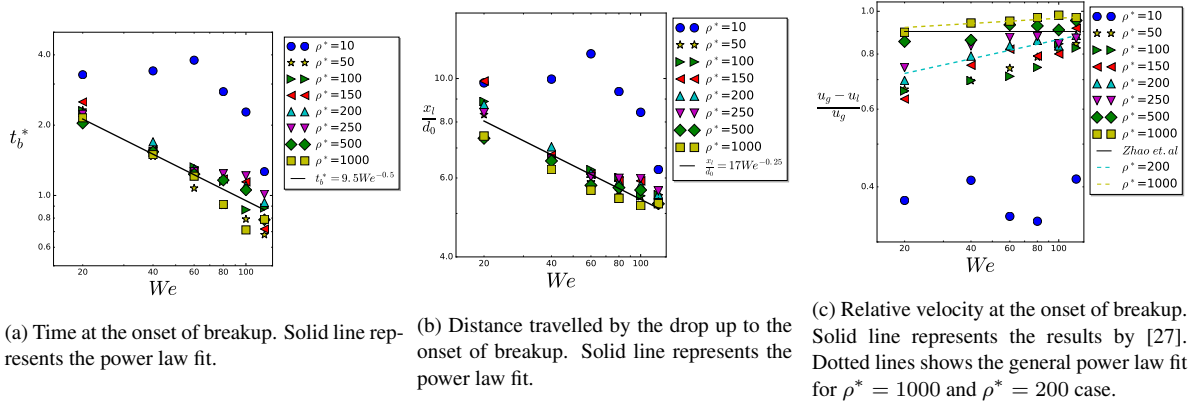


Figure 6: Relative velocities, time taken and the distance travelled by the drop at the onset of breakup for the parameters listed in the Table 2.

influenced by the surrounding gas flow [8]. Hence, drops for roughly $\rho^* \geq 150$ behave similarly at similar values of We . This difference in breakup for different ρ^* values (with Re_g , M being constant and $Oh < 0.1$) makes "Density Ratio" a crucial parameter in characterizing the secondary breakup of drops.

Figures 6a, 6b and 6c show the drop breakup time t_b^* , the drop displacement, x_l/d_0 , and the relative velocity of the centroid of the drop, $u_r = (U_g - u_l)/(U_g)$, respectively, at the onset of breakup for the conditions listed in the first row of the Table 2. Clearly, t_b^* and x_l/d_0 are quite different for the drops with $\rho^* = 10$ and for the drops with $\rho^* = 50 - 1000$. With an increase in We , both t_b^* and x_l/d_0 decrease following a power-law given by $t_b^* = 9.5We^{-0.5}$ and $x_l/d_0 = 17We^{-0.25}$, respectively. Relative velocity u_r on the other hand has a continuous variation from $\rho^* = 50$ to $\rho^* = 1000$ following a general power-law given by $4(10^{-4}\rho + 0.1)We^{(0.13-10^{-4}\rho)}$ with average values increasing from 0.76 to 0.95, though it is significantly different for $\rho^* = 10$ with an average value of 0.36. [27] reported an average value of 0.9 for ethanol and water drops combined, which are in good agreement with the simulations presented here (also shown in the figure as a line) and [28] reported 0.87 for water drops. Relative velocity, u_r , increases with an increase in ρ^* value indicating that the drops for lower ρ^* would attain higher velocity at the onset of breakup. Here, we note that the drops for $\rho^* = 10$ at $We = 20$ and 40 and for $\rho^* = 50$ at $We = 20$, do not breakup at all. This is in good agreement with the observations of [10]. The values corresponding to these values of ρ^* and We reported in the Figure 6 indicate only a tendency to breakup. This tendency to breakup is based on the criteria that the drop could have pinched-off at the thinnest section attained during the deformation process. However, when the simulations are run for a longer duration, the rim retracts and the breakup does not occur.

Summary and Conclusions

In the present study, we performed fully resolved numerical simulations of a drop in a high speed gas flow to investigate the effect of density ratio on the secondary breakup of the drops. These simulations were performed for a moderate Weber number range (20-120), where bag breakup, multi-mode and sheet-thinning breakup modes have been observed in experiments. Previous studies reported conflicting views on the effect of density ratio on the breakup modes and drop morphology [11, 12, 13]. To resolve these discrepancies, we performed a large set of simulations with different values of ρ^* from 10 to 1000, and We from 20 to 120. We found that the drops for $\rho^* < 150$ behave differently from $\rho^* \geq 150$ at the same We , making "Density ratio" an important parameter in characterizing secondary breakup of drops and also in the study of liquid jets in gas crossflow [29].

References

- [1] M. Pilch and C.A. Erdman. Use of breakup time data and velocity history data to predict the maximum size of stable fragments for acceleration-induced breakup of a liquid drop. *International Journal of Multiphase Flow*, 13(6):741 – 757, 1987.
- [2] G.M Faeth, L.-P Hsiang, and P.-K Wu. Annual reviews in multiphase flow 1995 structure and breakup properties of sprays. *International Journal of Multiphase Flow*, 21:99 – 127, 1995.
- [3] R D Guildenbecher. Secondary atomization. *Experiments in Fluids*, pages 371–402, 2009.
- [4] L.-P. Hsiang and G.M. Faeth. Near-limit drop deformation and secondary breakup. *International Journal of*

- Multiphase Flow*, 18(5):635 – 652, 1992.
- [5] W.-H. Chou and G.M. Faeth. Temporal properties of secondary drop breakup in the bag breakup regime. *International Journal of Multiphase Flow*, 24(6):889 – 912, 1998.
 - [6] M. Jain, R. S. Prakash, G. Tomar, and R. V. Ravikrishna. Secondary breakup of a drop at moderate Weber numbers. *Proceedings of the Royal Society A: Mathematical, Physical and Engineering Sciences*, 471(2177):20140930–20140930, 2015.
 - [7] A. B. Liu and Rolf D. Reitz. Mechanisms of air-assisted liquid atomization. *Atomization and Sprays*, 3(1):55–75, 1993.
 - [8] Suhas S Jain, Neha Tyagi, R Surya Prakash, R V Ravikrishna, and Gaurav Tomar. Secondary breakup of drops at moderate weber numbers: Effect of density ratio and reynolds number. *arXiv:1803.02989*, 2018.
 - [9] Stéphane Zaleski, Jie Li, and Sauro Succi. Two-dimensional navier-stokes simulation of deformation and breakup of liquid patches. *Phys. Rev. Lett.*, 75:244–247, Jul 1995.
 - [10] J. Han and G. Tryggvason. Secondary breakup of a axisymmetric liquid drops. II. Impulsive acceleration. *Physics of Fluids*, 13(6):1554–1565, 2001.
 - [11] C Aalburg, B van Leer, and G M Faeth. Deformation and drag properties of round drops subjected to shock-wave disturbances. *AIAA Journal*, 41, 2003.
 - [12] T Kékesi, G Amberg, and L Prah Wittberg. Drop deformation and breakup. *International Journal of Multiphase Flow*, 66:1–10, 2014.
 - [13] Wei Yang, Ming Jia, Kai Sun, and Tianyou Wang. Influence of density ratio on the secondary atomization of liquid droplets under highly unstable conditions. *Fuel*, 174:25 – 35, 2016.
 - [14] Feng Xiao, M. Dianat, and James J. McGuirk. Large eddy simulation of single droplet and liquid jet primary breakup using a coupled level set/volume of fluid method. *Atomization and Sprays*, 24(4):281–302, 2014.
 - [15] F. Xiao, M. Dianat, and J.J. McGuirk. A robust interface method for drop formation and breakup simulation at high density ratio using an extrapolated liquid velocity. *Computers & Fluids*, 136:402 – 420, 2016.
 - [16] Sachin Khosla, Clifford E Smith, and Ryan P Throckmorton. Detailed understanding of drop atomization by gas crossflow using the volume of fluid method. In *ILASS Americas, 19th Annual Conference on Liquid Atomization and Spray Systems, Toronto, Canada*, 2006.
 - [17] Shahab Mirjalili, Suhas S Jain, and Micheal Dodd. Interface-capturing methods for two-phase flows: An overview and recent developments. *Annual Research Briefs*, pages 117–135, 2017.
 - [18] J.U Brackbill, D.B Kothe, and C Zemach. A continuum method for modeling surface tension. *Journal of Computational Physics*, 100(2):335 – 354, 1992.
 - [19] Stephane Popinet. Gerris: a tree-based adaptive solver for the incompressible euler equations in complex geometries. *Journal of Computational Physics*, 190(2):572 – 600, 2003.
 - [20] Stephane Popinet. An accurate adaptive solver for surface-tension-driven interfacial flows. *Journal of Computational Physics*, 228(16):5838 – 5866, 2009.
 - [21] Gaurav Tomar, Daniel Fuster, Stephane Zaleski, and Stephane Popinet. Multiscale simulations of primary atomization. *Computers & Fluids*, 39(10):1864 – 1874, 2010.
 - [22] Marianne M. Francois, Sharen J. Cummins, Edward D. Dendy, Douglas B. Kothe, James M. Sicilian, and Matthew W. Williams. A balanced-force algorithm for continuous and sharp interfacial surface tension models within a volume tracking framework. *Journal of Computational Physics*, 213(1):141 – 173, 2006.
 - [23] Stefan A. Krzeczowski. Measurement of liquid droplet disintegration mechanisms. *International Journal of Multiphase Flow*, 6(3):227 – 239, 1980.
 - [24] L. Rayleigh. On the capillary phenomena of jets. *Proceedings of the Royal Society I.*, 29(196-199):71–97, 1879.
 - [25] Jaehoon Han and Gretar Tryggvason. Secondary breakup of axisymmetric liquid drops. I. Acceleration by a constant body force. *Physics of Fluids*, 11(12):3650, 1999.
 - [26] Suhas S Jain, Neha Tyagi, Gaurav Tomar, Surya R Prakash, and R V Ravikrishna. Effect of density ratio on the secondary breakup of spherical drops in a gas flow. *Proceedings of 18th Annual Conference of Liquid Atomization & Spray Systems - Asia*, 2016.
 - [27] Hui Zhao, Hai Feng Liu, Wei Feng Li, and Jian Liang Xu. Morphological classification of low viscosity drop bag breakup in a continuous air jet stream. *Physics of Fluids*, 22(11), 2010.
 - [28] Z. Dai and G.M. Faeth. Temporal properties of secondary drop breakup in the multimode breakup regime. *International Journal of Multiphase Flow*, 27(2):217 – 236, 2001.
 - [29] Surya R Prakash, Suhas S Jain, Gaurav Tomar, R V Ravikrishna, and B N Raghunandan. Computational study of liquid jet breakup in swirling cross flow. *Proceeding of 18th Annual Conference of Liquid Atomization & Spray Systems - Asia*, 2016.